Mechanisms of Frictional Energy Dissipation at Graphene Grain Boundaries

Supplemental Material

Xiang Gao, Wengen Ouyang, Oded Hod, and Michael Urbakh

Department of Physical Chemistry, School of Chemistry, The Raymond and Beverly Sackler Faculty of Exact Sciences and The Sackler Center for Computational Molecular and Materials Science, Tel Aviv University, Tel Aviv 6997801, Israel.

In this supporting information, we provide additional details on certain aspects of the study reported in the manuscript. The following issues are discussed:

1. Atomic Structures of Common Dislocations in Graphene

2. Effect of Out-of-Plane Deformation on Stress Field Relaxation

3. Atomic Structures and Topography of GBs with Respect to Misfit Angle

4. Calculation of GB Energy

5. Comparison of GB Energies of Corrugated and Flat GBs

6. Effect of Scan Line on Friction

7. Temperature Effect on GB Friction

8. Nudged Elastic Band Calculations of the Elastic Energy

9. Calculation of Instantaneous Buckling Velocity

10. Kinetic Energy Change with Bump Buckling

11. Effect of Sliding Velocity on Bump Buckling/Unbuckling

12. Additional Sliding Simulation Results

13. Potential Energy Analysis

14. Sensitivity Analysis of the Damping Rate Applied to the Top Layer of the Flake

1. Atomic Structures of Common Dislocations in Graphene

All the grain boundaries (GBs) generated in this study were constructed by three types of pentagon-heptagon (5|7) dislocations that can be described with the Burgers vector, $\vec{b}$, which is a topological invariant of the dislocation and a translational vector of graphene lattice, $i.e.$ $\vec{b} = m\vec{a}_1 + n\vec{a}_2$, where m, n are a pair of integers and $\vec{a}_1$, $\vec{a}_2$ are the graphene lattice vectors [1]. The pair of integers (m,n) is commonly used to denote the type of (5|7) dislocations, in analogy to the chiral indices of carbon nanotubes. In Fig. S1, we show the atomic structures of three common types of (5|7) dislocations marked as (1,0), (1,1) and (2,0), which have been widely observed in experiments [2,3]. The dislocation can be viewed as the result of inserting a semi-infinite ribbon of width $|\vec{b}|$ into the otherwise perfect graphene lattice [1]. The (1,0) dislocation has the shortest Burgers vector, $|\vec{b}| = $ 2.46 Å. The (0,1) dislocation, with a same length ($|\vec{b}| = $ 2.46 Å.), differs from the (1,0) dislocation only in the direction of the Burgers vector (by 60°). Here, both (1,0) and (0,1) dislocations are referred as (1,0) type dislocations. A similar notation is used for (2,0) and (0,2) dislocations that both are referred as (2,0) type dislocations. The (1,1) dislocation has the second shortest Burgers vector $|\vec{b}| = $ 4.26 Å and the (2,0) dislocation has a Burgers vector that is twice as long as that of the (1,0) dislocation.

(1,0) dislocation   (1,1) dislocation   (2,0) dislocation
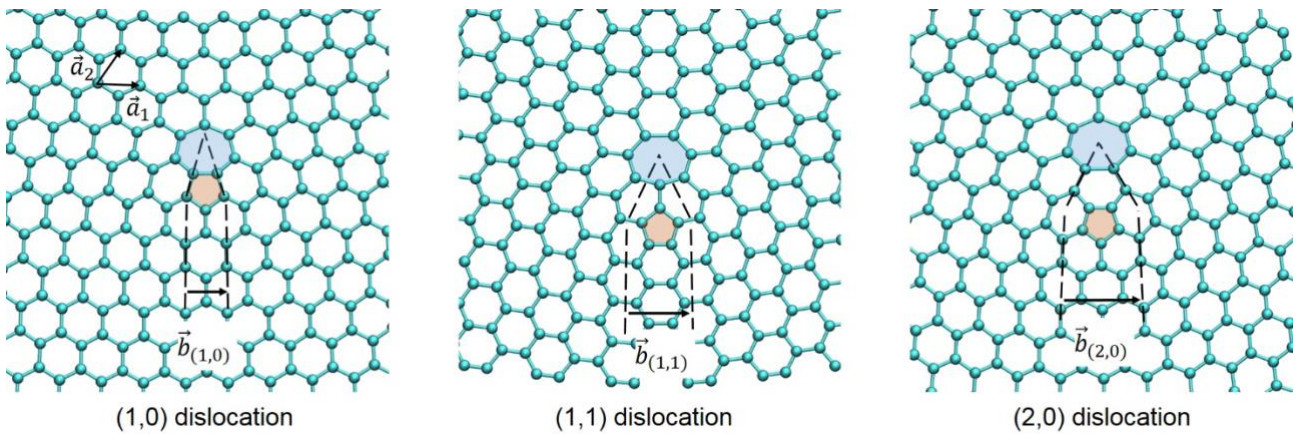
FIG. S1. Atomic structures of (1,0), (1,1) and (2,0) dislocations. The pentagon and heptagon defects are filled with light orange and light blue, respectively. The dashed lines outline the inserted semi-infinite graphene ribbons. For clarity of the presentation, the Burgers vectors of the three illustrations are aligned in the same direction.

2. Effect of Out-of-Plane Deformation on Stress Field Relaxation

To explain why some GB structures result in corrugated seam lines we performed geometry optimization with and without out-of-plane relaxation for the $\theta = 9.7°$ GB [Fig. 1(a) of the main text] and studied the corresponding in-plane stress field. Fig. S2 shows the color maps of the distribution of C-C bond length and in-plane stress with and without out-of-plane deformation. For the case without out-of-plane deformation (left column), the atoms in the polycrystalline graphene are relaxed only in lateral directions, whereas for the case with out-of-plane deformation (right column), the atoms in the polycrystalline graphene are allowed to relax in all three directions. The relaxation protocol is the same as that described in the Method section of the main text.

It is seen that, without out-of-plane deformation, the dislocations in the GB lead to strongly compressed and stretched regions alternately distributed along the GB [Figs. S2(a), S2(e), and S2(g)]. The compressed regions and the stretched regions correspond to the pentagons and heptagons of the dislocations (see Section 1 above), respectively. With out-of-plane deformation, the compressed pentagons protrude upward forming surface bumps [Figs. S2(c)-S2(d)]. Correspondingly, the compressed C-C bond length and the compressive in-plane stress at the pentagons are significantly relaxed [Figs. S2(b), S2(f), and S2(h)].

The dependence of the bump height on the GB misfit angle θ can be rationalized considering the alternating compressed and stretched regions in the vicinity of the GB seam. The stress field of a dislocation consists of compression on the pentagon side and tension on the heptagon side, which is relieved by the stress fields of its neighboring dislocations. As θ increases, the distance between neighboring dislocations decreases, therefore promoting the stress tension cancellation. This effect is enhanced when the two dislocations are directly connected through sharing a C-C bond, hexagon ring, or a pair of mutual edge atoms. Thus, the bump height decreases with increasing θ, and the bumps can be even annihilated when directly connected to their neighboring dislocations.

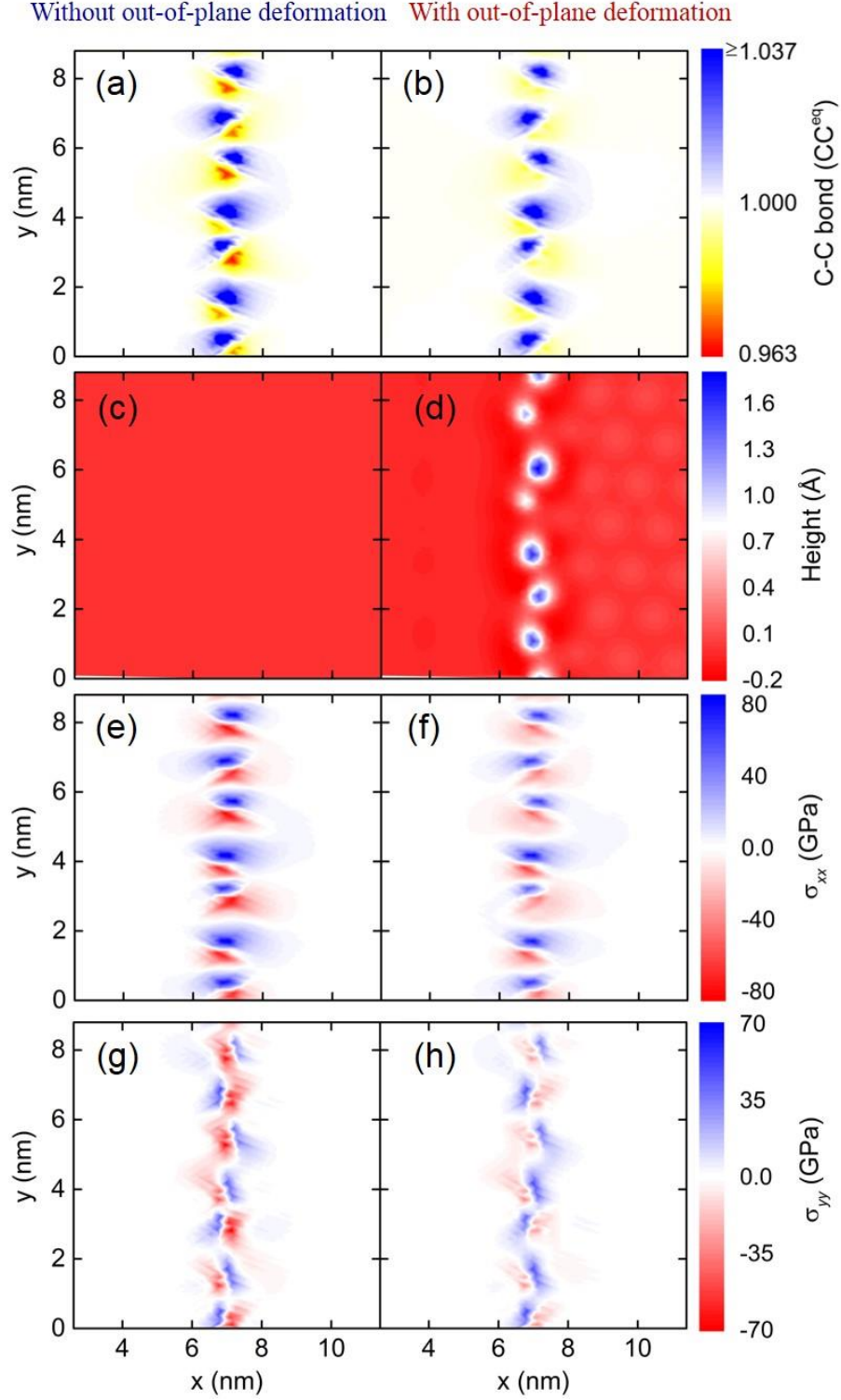**FIG. S2.** Effect of out-of-plane deformation on the stress field relaxation for a $\theta = 9.7°$ GB. (a)–(b) the bond length distribution; (c)-(d) height distribution, (e)-(f) x-axis stress distribution, and (g)-(h) y-axis stress distribution. Panels in the left column are relaxed without allowing for out-of-plane deformation whereas panels in the right column are relaxed allowing for out-of-plane deformation. The C-C bond length is normalized by the equilibrium carbon-carbon distance in an isolated pristine graphene surface, $a_{CC} = 1.42039$ Å. Using the procedure described in Ref. [4], the stresses are calculated from the global stress tensor obtained from LAMMPS divided by the atomic volume of carbon atoms. The latter is evaluated with $3\sqrt{3}a_{CC}h/4$, where $h = 3.35$ Å is the equilibrium interlayer distance.

3. Atomic Structures and Topography of GBs with Respect to Misfit Angle

Figure S3 reports a series of atomic structures and topography of Corrugated-I GBs [corrugated with only (1,0) type dislocations] with misfit angles $\theta = 3.3°$, $6.6°$, $12.5°$, $18.1°$ and $24.3°$, respectively. As θ increases, the density of dislocations increases while the height of bumps drops due to stress field cancellation discussed in Section 2. For $\theta < 12.5°$, the bump density D increases linearly with θ as each dislocation generates a surface bump. While for $\theta \geq 12.5°$, the dislocations start to connect directly with each other through sharing a C-C bond, hexagon carbon ring, or a pair of mutual edge atoms, which significantly reduces the local stress field and annihilates bumps. Thus, the bump density decreases with increasing θ in this angle range. Flat GBs [with a typical surface corrugation lower than 0.2 Å as shown in Fig. 2(a) in the main text] are observed at misfit angles of $\theta = 21.8°$, $25.7°$, $27.8°$ and $30°$. Flat-I GBs [flat with only (1,0) type dislocations] are observed at all the four misfit angles, while Flat-II GBs [flat with (1,0) type dislocations mixed with (1,1) or (2,0) type dislocations] are only found at $\theta = 27.8°$ [with (1,1) type dislocation]. For the flat $\theta = 21.8°$ GB, the dislocations are connected with each other by sharing a C-C bond, a hexagon carbon ring, or a pair of mutual edge atoms. For the flat $\theta = 25.7°$ and $27.8°$ GBs, the dislocations are arranged by sharing a C-C bond or a pair of mutual edge atoms. While for $\theta = 30°$, the dislocations form a fully edge-sharing dislocation chain.
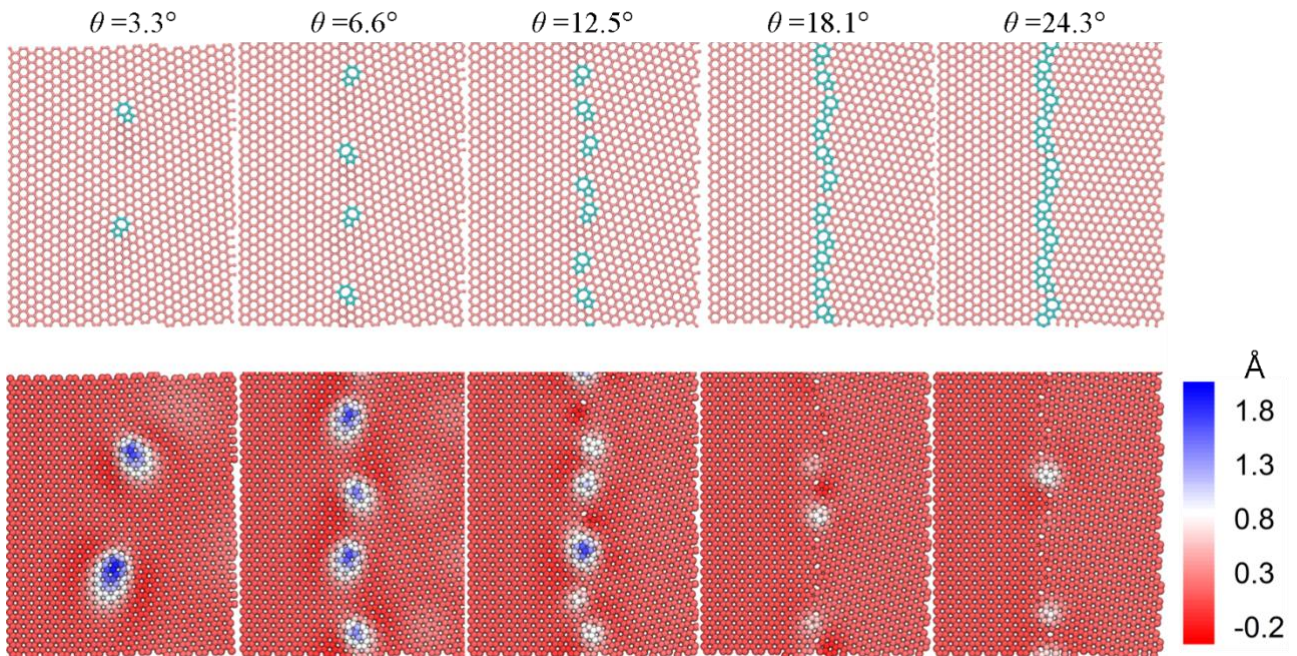

FIG. S3. Atomic structures and topography for corrugated GBs (Corrugated-I) at misfit angles of $\theta = 3.3°$, $6.6°$, $12.5°$, $18.1°$ and $24.3°$, respectively. Panels in the top row show the atomic structures of GBs on a graphite substrate after annealing. Panels in bottom row report the corresponding topography (height distribution) of the GBs in the top row. The color of atoms represents the atomic height with respect to the average height of the two grains.

The appearance of flat GB at misfit angles of θ = 21.8°, 25.7°, 27.8° and 30° is consistent with previous density functional theory calculations of free standing polycrystalline graphene at GB misfit angles of 21.8°, 32.2° and 38.2° [1], as well as STM measurement of graphene supported on a SiC substrate with misfit angle in the range of 25° < θ < 40° [5].

In addition, for the four misfit angles where flat GBs appear, when the stress field is not sufficiently cancelled along the GB seamline corrugated GBs (Corrugated-I and Corrugated-II) can also form. Fig. S4, shows four examples of such corrugated GBs.
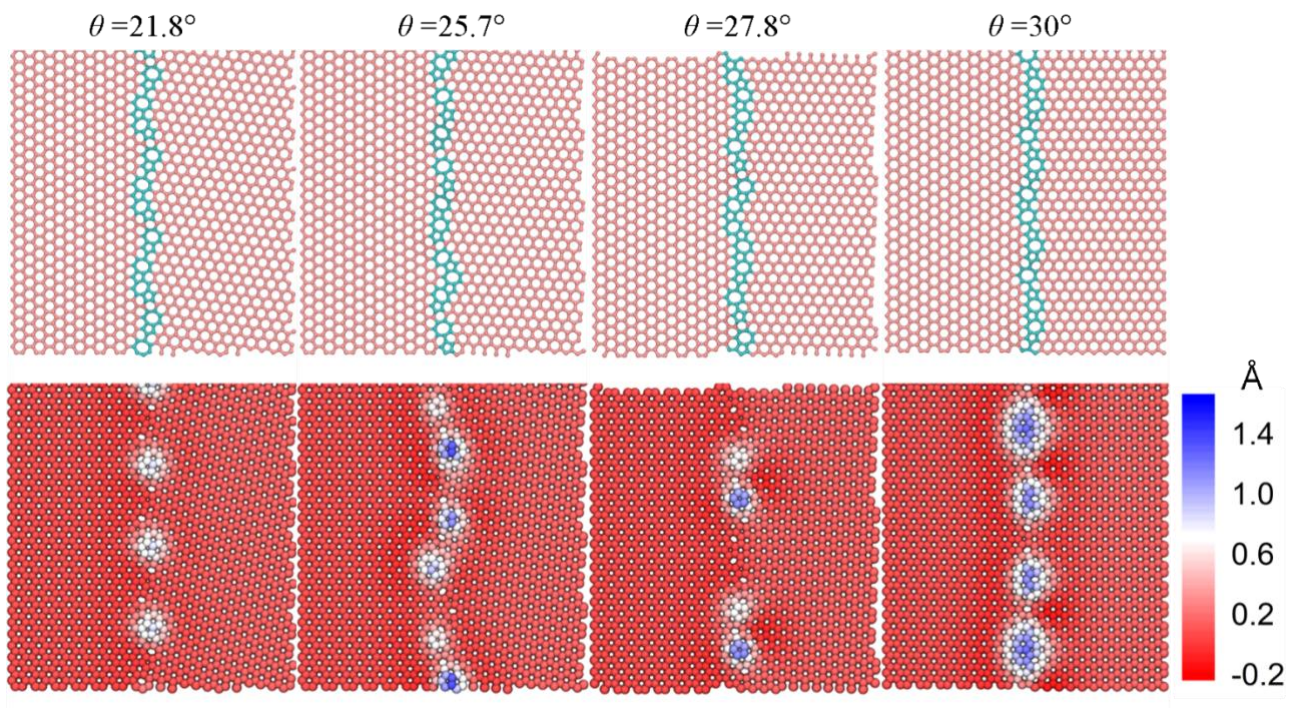

FIG. S4. Atomic structures and topography of corrugated GBs (Corrugated-I and Corrugated-II) at misfit angles of θ = 21.8°, 25.7°, 27.8° and 30°, respectively. Panels in top row show the atomic structures for GBs on a graphite substrate after annealing. Panels in the bottom row present the corresponding topography of the GBs in the top row. The color represent the atomic height with respect to the average height of the two grains.

4. Calculation of GB Energy

To evaluate the GB energy per unit length, γ, we adopt the approach used in Ref. [2], where $\gamma = (E_{\text{total}} - n_{\text{atoms}} \times \bar{E}_{\text{bulk}})/l_{\text{GB}}$. Here E_{total} is the total potential energy of the atoms in the polycrystalline graphene layer, n_{atoms} is the total number of atoms in the polycrystalline graphene layer, $\bar{E}_{\text{bulk}} \approx 7.42$ eV (Fig. S5) is the average potential energy per atom in the bulk regions of Grain 1 and Grain 2, and l_{GB} is the length of the GB. The calculated GB energy per unit length $\gamma = 0 - 0.5$ eV/Å is comparable to that obtained for buckled GBs in free-standing polycrystalline graphene $\left(\gamma = 0 - 0.4 \text{ eV/Å}\right)$ [1].
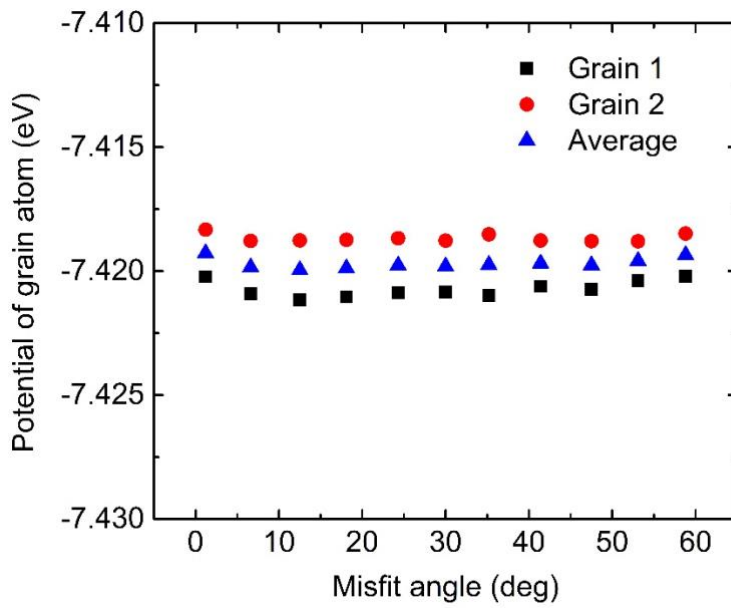

FIG. S5. The potential energy per atom in the bulk regions of the two grains and their average as a function of misfit angle.

5. Comparison of GB Energies of Corrugated and Flat GBs

In Fig. 2 of the main text, the energies of the Corrugated-I and Flat-I GBs are roughly identical. The reason is that, after geometry relaxation, the GB energy is mainly determined by the type [e.g. (1,0), (1,1), or (2,0) type] and density of the dislocations. For Corrugated-I and Flat-I GBs with same misfit angle, the type and density of dislocations are similar, as shown in Fig. S6. Prior to geometry relaxation, Flat-I type GBs show lower energy than their Corrugated-I counterparts, because the latter exhibits larger in-plane stress. Following relaxation, the in-plane stress is partially released and the energy of the Corrugated-I GBs decreases, approaching the value of Flat-I GBs. A similar picture arises for the Corrugated-II and Flat-II GBs. To exemplify this effect, we calculated the energy of the $\theta = 21.8°$ Corrugated-I GB. For this system, the GB energy drops from 0.51 eV/Å prior to geometry relaxation to 0.46 eV/Å following relaxation. The latter is close to the GB energy of the Flat-I GB with the same misfit angle.
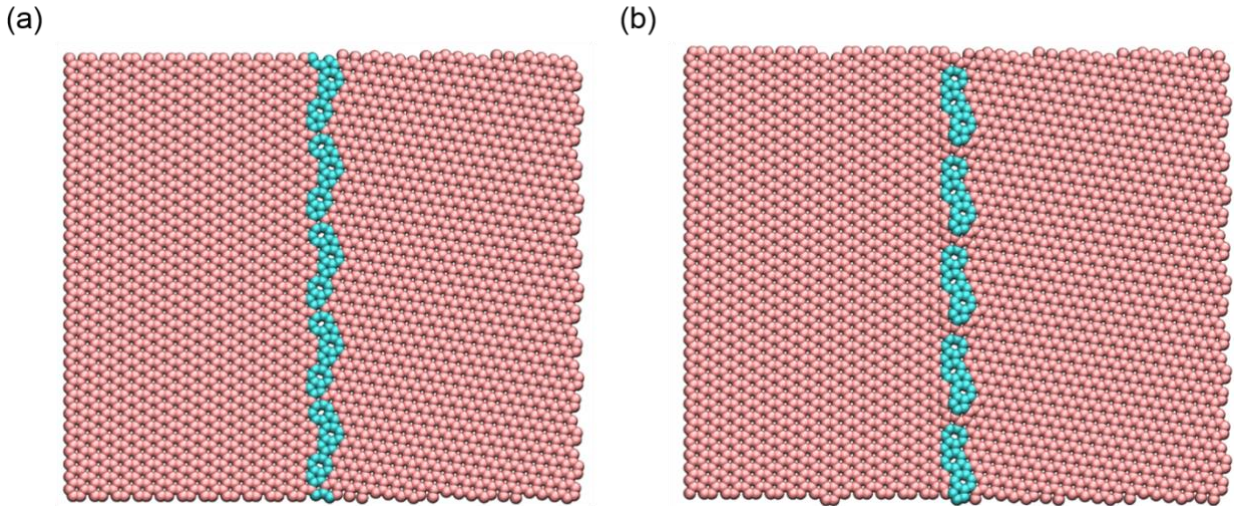

FIG. S6. Atomic structures of (a) a Flat-I GB and (b) a Corrugated-I GB with a misfit angle $\theta = 21.8°$. The cyan and pink spheres represent the pentagon-heptagon dislocation atoms and hexagonal carbon atoms, respectively.

6. Effect of Scan Line on Friction

The scanline for the $\theta = 4.7°$ GB was deliberately chosen so that the flake would slide over a single GB bump avoiding interaction with adjacent bumps. This allowed us to assess the effects of a single GB defect on the frictional properties of the system. To examine the effect of scanning off-center with respect to a GB defect, we chose a scanline shifted downwards by 5 Å along the GB axis with respect to the original one [see Figs. S7(a)-S7(b)]. Along this scan line the flake is still strongly influenced by the original bump but has some overlap with the adjacent bump. For comparison purposes, we performed simulations at representative normal loads of 0, 0.8, and 2.3 GPa. Similar to the results obtained along the original scan line, we observe bump buckling at both 0.8 and 2.3 GPa but not at 0 GPa. The comparison of frictional stresses between the original scan line and shifted scan line are shown in Figs. S7(c)-S7(e), for forward sliding, backward sliding, and their average, respectively. It can clearly be seen that there is good qualitative agreement between the original and the new results. Therefore, we conclude that the scan line has minor effect on the general qualitative frictional behavior of the system and on the underlying mechanisms.
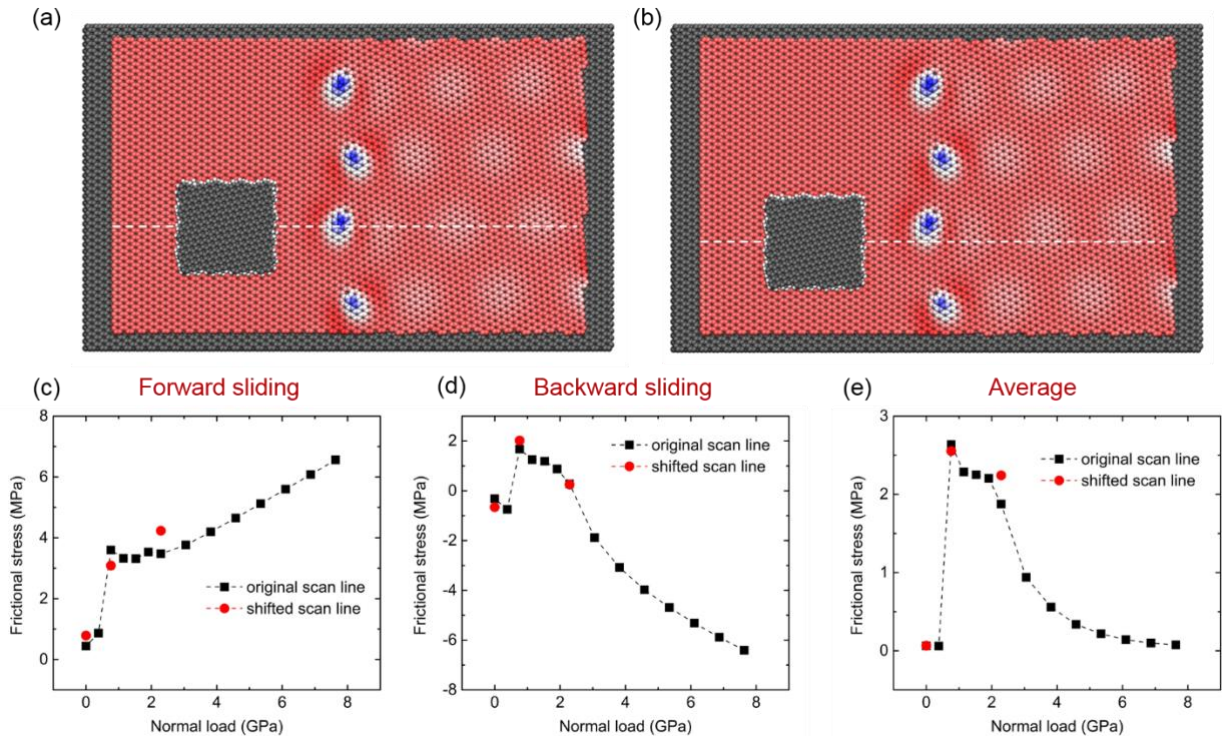

FIG. S7. Effect of the slider scan-line on the friction. (a) Model system of misfit angle $\theta = 4.7°$ with the scan line (dashed white) used in the main text. (b) Same as (a) with a scan line shifted downward by 5 Å. (c)-(e) Comparison of the frictional stresses obtained using the original scan line in (a) and shifted scan line in (b), as a function of normal load in the forward and backward sliding directions and their average, respectively.

7. Temperature Effect on GB Friction

To demonstrate the temperature effect on the GB friction, we performed forward sliding simulations over the $\theta = 4.7°$ GB at 300 K. The comparison of the shear stress at 0 K and 300 K is shown in Fig. S8. Generally, the shear stress at 300 K behaves similar to the 0 K case. At low normal loads (< 1.5 GPa), the shear stress increases rapidly with normal load and roughly follows the results of 0 K. This effect is dominated by bump buckling events at both temperatures considered. At the high normal load regime (> 4 GPa), the shear stress is slightly higher than that calculated at 0 K, showing a similar increase with the normal load. We note that at 300 K the critical normal load for bump buckling is reduced to nearly zero and the frequency of buckling events is enhanced due to thermal fluctuation.
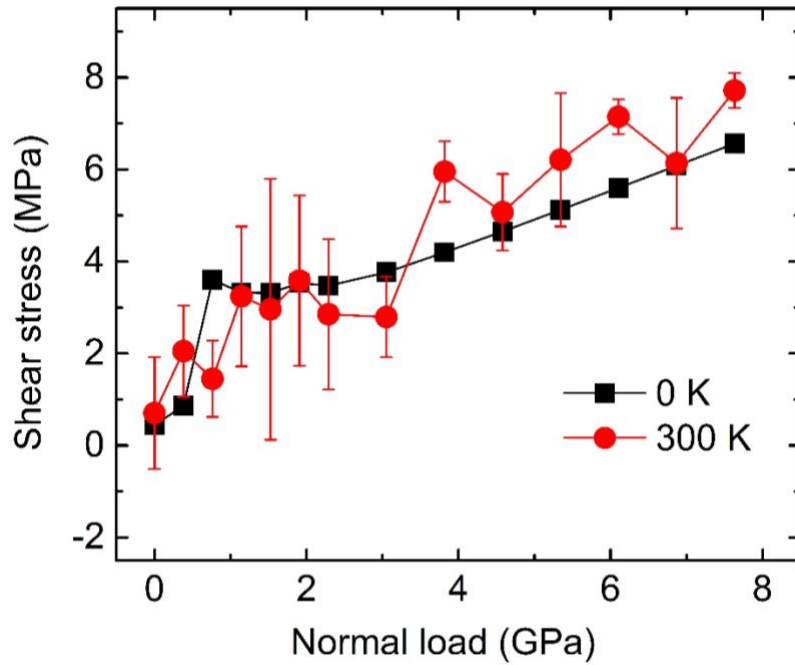

FIG. S8. Shear stress in forward sliding over the $\theta = 4.7°$ GB at 0 K and 300 K as a function of normal load. The error bars for 300 K are obtained by averaging three individual simulations with different initial conditions.

8. Nudged Elastic Band Calculations of the Elastic Energy

To evaluate the amount of elastic energy that can be stored in the GB due to buckling and the corresponding barriers we performed nudged elastic band (NEB) calculations [6-10] along individual bump buckling reaction coordinate for the corrugated GBs considered in the absence of the sliding flake (see details in the Method section 5). Figure S9(a) presents the buckling potential energy profile for $\theta = 4.7°$ GB, where the insets show the configuration of the (a) unbuckled, (b) transition, and (c) buckled states. The energy barrier for downward buckling is found to be ~0.9 eV explaining the abovementioned normal load threshold required for buckling to occur. The considerably lower (~0.1 eV) unbuckling barrier explains why buckling is found to be reversible in many of our dynamic simulations. We note however, that dynamical effects in the presence of the sliding flake can results in irreversible buckling (see SM Movie 4), leading to the loss of energy towards elastic degrees of freedom, therefore enhancing friction.

For the $\theta = 13.9°$ high bump density GB case a somewhat more involved picture arises. Here, the sliding area contains more than one bump and hence several reaction paths can be envisioned exhibiting different bump buckling sequences. Two such sequences are demonstrated in Figs. S9(b) and S9(c) where the reaction paths, barriers, and corresponding geometries depend on which of the two bumps residing in the sliding path buckles first.
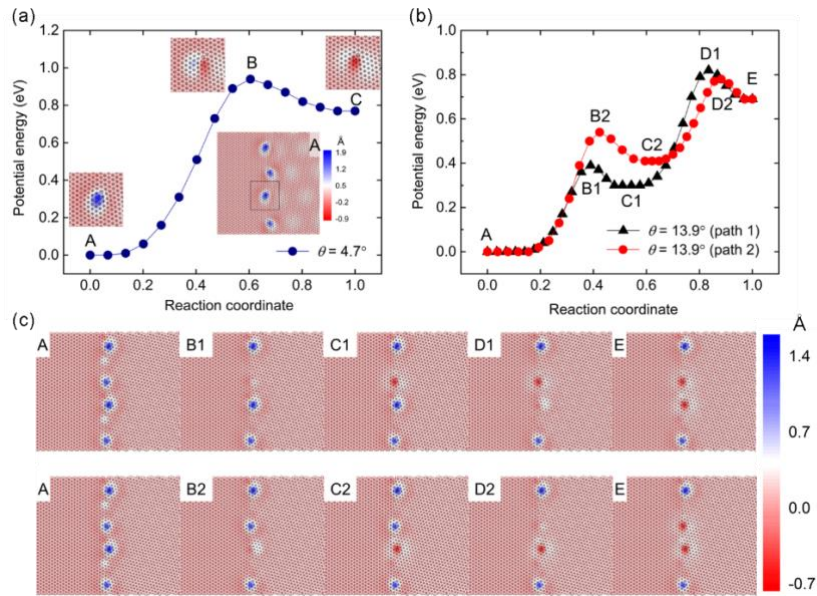

FIG. S9. NEB calculations. (a) Potential energy of the system along the reaction coordinate for the $\theta = 4.7°$ GB buckling without the TLG flake. The black square in the inset marks the bump which resides along the sliding path. The zoomed-in snapshots are displayed near each minimum and the transition state. (b) Potential energy of the system along the reaction coordinate for the $\theta = 13.9°$ GB. (c) The snapshots for each minimum and transition state appearing in (b). The lowest energy state along the buckling reaction coordinates for both systems are shifted to zero for clarity of the presentation. The color scales denote the atomic height with respect to the average height of the two grains.

9. Calculation of Instantaneous Buckling Velocity

The instantaneous bump velocity in the vertical direction v_t at time t is calculated as $v_t = \frac{1}{\Delta t}\left(z_{t+\Delta t/2} - z_{t-\Delta t/2}\right)$, where Δt is the time interval, and $z_{t+\Delta t/2}$ and $z_{t-\Delta t/2}$ are the z coordinates of the peak atom of the bump (chosen at the initial configuration) at time $t + \Delta t/2$ and $t - \Delta t/2$, respectively. The calculated velocity profiles with different time intervals for a buckling event are shown in Fig. S10. In the region away from the buckling position, a time interval of 1 ps is used (not to be confused with the simulation time-step of 1 fs), which shows minor effect on the velocity calculation. While in the buckling region, the fast motion associated with the buckling process is not well captured using the same time interval, which significantly underestimates the instantaneous buckling velocity. To provide sufficient numerical accuracy of the bump buckling simulation, we used a 100 fs time interval to calculate the instantaneous velocity in the vicinity of the buckling region. Then, the full velocity profile is built by combining the parts in the buckling region and away from the buckling region.
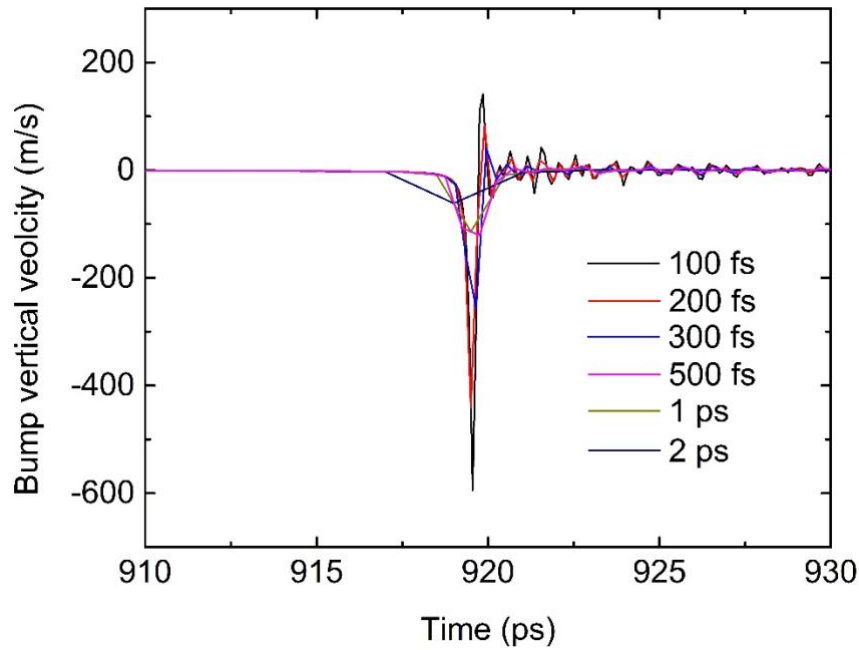

FIG. S10. Instantaneous velocity profiles for a buckling event calculated using different time intervals for the $\theta = 4.7°$ GB at a normal load of 0.8 GPa.

10. Kinetic Energy Change with Bump Buckling

Figure S11(a) shows the typical kinetic energy change of the system during a buckling event. The total kinetic energy jumps up suddenly at certain point and then gradually drops with some fluctuations. The sudden jump of the total energy results from the instantaneous buckling velocity (as high as ~600 m/s under our simulation conditions), as shown in Fig. 4(b) in the main text. To further illustrate this, we calculate separately the kinetic energy components of the flake, in the bump region and non-bump region, as illustrated in Fig. S11(b). The bump region is defined as a circular region centered at the peak atom of the bump (chosen at the initial state) with a radius of 1 nm [sufficiently large to cover most of the bump region based on the height profile while avoiding overlap with other bumps, as shown in Fig. S11(c)]. The atoms in the same circular region in the layer below the polycrystalline graphene are also included in the bump region. The rest of the substrate is defined as the "non-bump" region. The assignment of atoms to the two regions is made according to the initial state and remains unchanged during the simulation. As shown in Fig. S11(b), a kinetic energy spike is first generated in the bump region, and then it transfers to the flake and non-bump region. The dissipation of this kinetic energy pulse lasts for ~5 ps. This clearly supports the argument that the pulse in total kinetic energy of the system is caused by bump buckling.
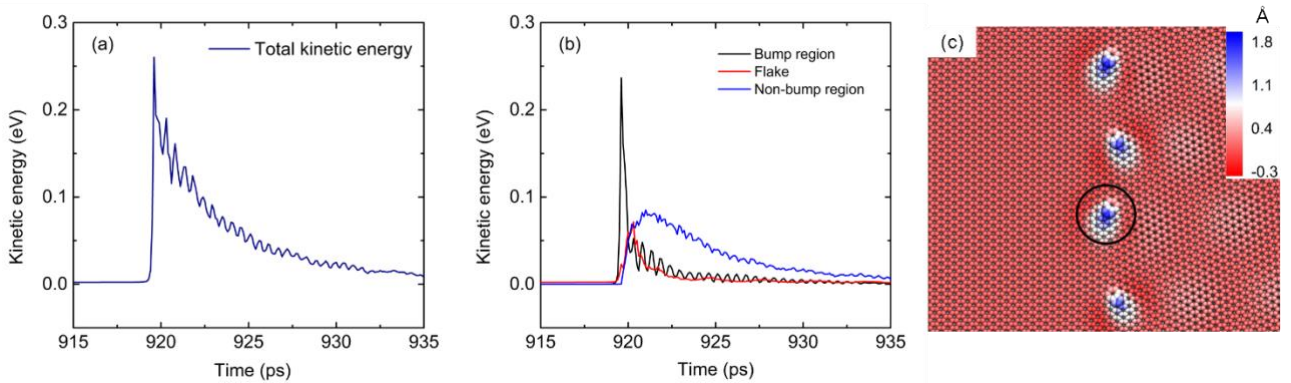

FIG. S11. Kinetic energy variations during a buckling event for the $\theta = 4.7°$ GB under a normal load of 0.8 GPa. (a) Total kinetic energy of the system. (b) Kinetic energy of the bump region, the flake, and "non-bump" region. (c) Definition of the bump region, which is outlined with the black circle. The colors of the atoms represent the vertical height of the atoms above the average height of the two grains.

13

11. Effect of Sliding Velocity on Bump Buckling/Unbuckling

To investigate the sliding velocity effect on the bump buckling dynamics, we performed quasi-static simulations (see Methods section 4 in the main text) with the $\theta = 4.7°$ GB system under normal loads of 0.4 GPa (where buckling/unbuckling is not observed) and 0.8 GPa (where buckling/unbuckling is observed). Under a normal load 0.4 GPa, the comparison of lateral force traces obtained from dynamic simulation and quasi-static simulation [see Fig. S12(a)] shows good agreement both when the slider approaches the GB and when it leaves it, representing the stages that are most prone to abrupt dynamic buckling effects. The corresponding snapshots presented in Fig. S12(b), taken from the quasi-static trace, resemble the depression and recovery of the bump during the dynamic simulation. Under a normal load of 0.8 GPa (see Fig. S13) the quasi-static trace also shows good agreement with dynamic simulations results. We attribute this behavior to the fact that the buckling and unbuckling dynamics time-scale is much faster than the corresponding time required for the flake to cross the GB when pulled at a velocity of 5 m/s. Hence, we conclude that the bump buckling dynamics is insensitive to the sliding velocity in the range used in this study.
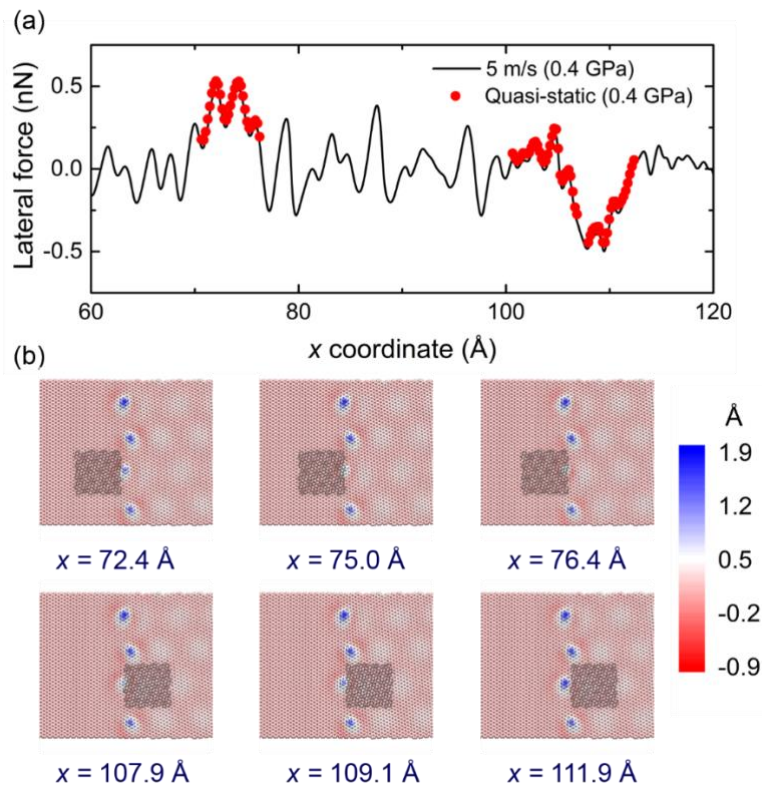

FIG. S12. Comparison of quasi-static and dynamic simulations results for the $\theta = 4.7°$ GB under a normal load of 0.4 GPa. (a) The lateral force traces. (b) Snapshots for the bump at different sliding positions along the quasi-static trace. The color of the spheres in the polycrystalline graphene layer represents the atomic height with respect to the average height of the two grains, using the color scale on the right. The grey spheres represent the carbon atoms residing in the bottom layer of the flake.
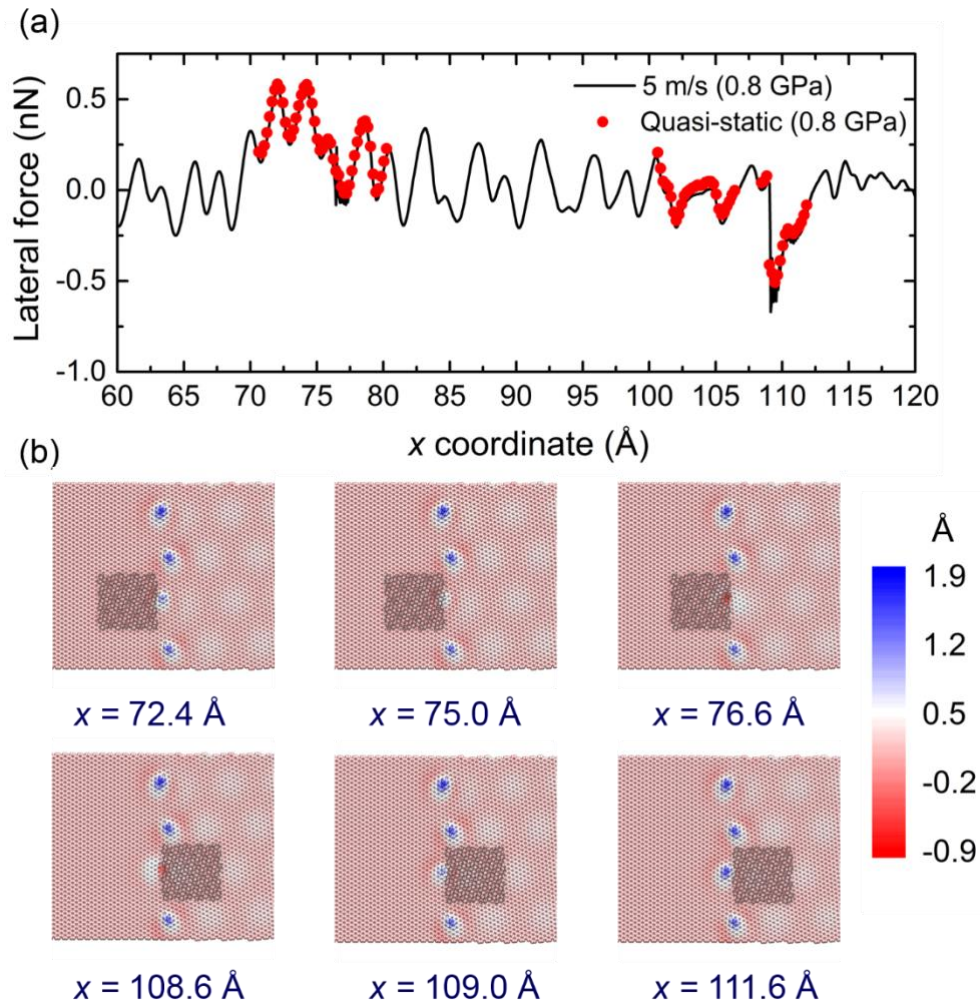
FIG. S13. Comparison of quasi-static and dynamic simulations results for the $\theta = 4.7°$ GB under a normal load of 0.8 GPa. (a) The lateral force traces. (b) Snapshots for the bump at different sliding positions along the quasi-static trace. The color of the spheres in the polycrystalline graphene layer represents the atomic height with respect to the average height of the two grains, using the color scale on the right. The grey spheres represent the carbon atoms residing in the bottom layer of the flake.

12. Additional Sliding Simulation Results

12.1. Backward Sliding over the corrugated $\theta = 4.7°$ GB

Following the forward sliding simulations, where the TLG flake is initially positioned over Grain 1 and pulled towards Grain 2, we performed backward sliding simulations starting from the endpoint located over Grain 2 and pulling the TLG flake towards Grain 1 along the same scanline and at the same pulling velocity of 5 m/s. The lateral force traces (left column) and bump dynamics (right column) at different normal loads during the backward sliding over the $\theta = 4.7°$ GB are shown in Fig. S14. In the backward sliding simulation, the bump was found to buckle at 0.8 GPa [see panels (c) and (d) of Fig. S14, and SM Movie 4], similar to the forward sliding case. However, in contrast to the forward sliding dynamics, for loads below 3 GPa the bump does not unbuckle but rather remains depressed even after the flake leaves the GB region [see panel (d) of Fig. S14, and SM Movie 4]. This is clearly reflected in the force trace at 0.8 GPa normal load in panel (c) of Fig. S14, where the flake experiences a resistive force when first encountering the GB (0.86-0.96 ns in the diagram) followed by force oscillations corresponding to the downward bump buckling (at simulation time of 0.96 ns). Notably, the negative lateral force observed in the forward sliding case [see Fig. 4(a) of the main text] at this pressure range due to bump unbuckling is lacking. At a normal load of 3 GPa the bump unbuckles after the TLG flake leaves the GB region resulting in sharp force spikes at simulation time of 1.67 ns, followed by force oscillations [see panels (e) and (f) of Fig. S14]. A similar behavior is found at higher normal loads, however since the unbuckling bump vertical velocity in this case is reduced, the sharp spikes observed at 3 GPa are replaced by smoother oscillations.

The different behavior between the forward and backward sliding dynamics can be attributed to the asymmetry of the bump structure with respect to the GB axis, where the pentagonal dislocation rings incline towards Grain 1 (see Fig. S15). We find that, once buckled, the bump is more likely to unbuckle when the flake leaves the GB from the heptagon side (*i.e.* in forward sliding direction) than when it leaves from the pentagon side (backward sliding direction).
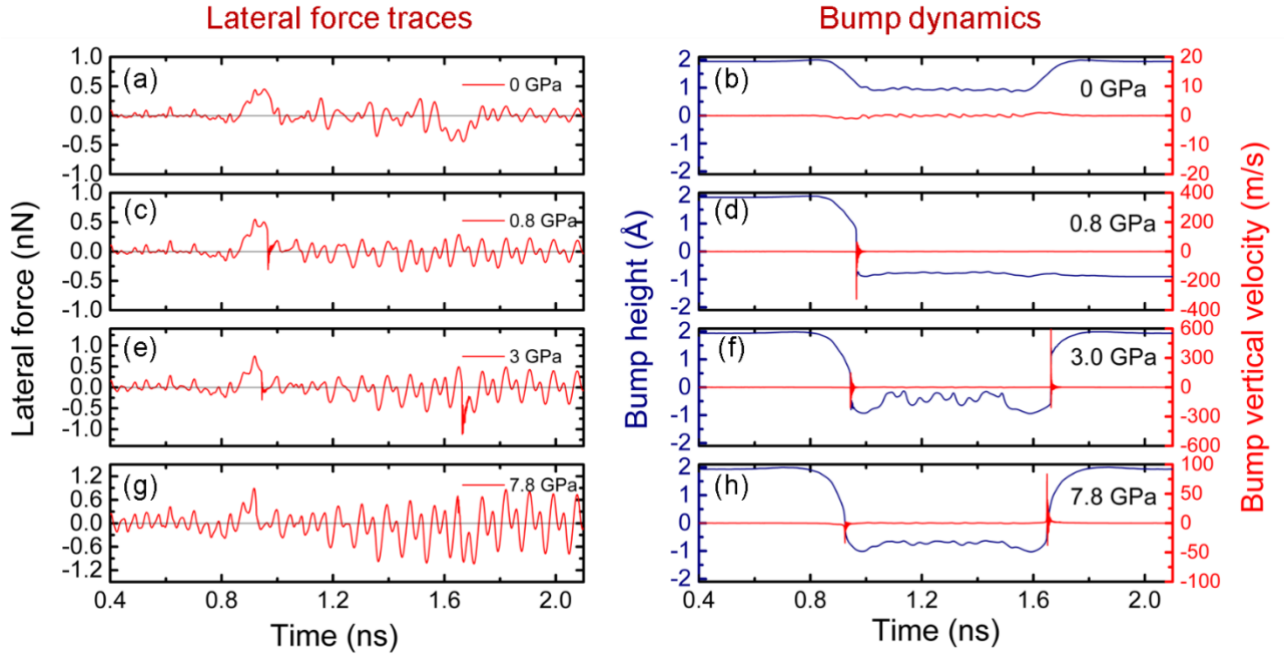
FIG. S14. Lateral force traces and bump dynamics in the backward sliding direction for the $\theta = 4.7°$ GB. Panels (a), (c), (e), and (g) present the lateral force traces as a function of time for normal loads of 0, 0.8, 3.0, and 7.8 GPa, respectively. Panels (b), (d), (f), and (h) show the corresponding bump heights and bump vertical velocities variation profiles. Positive values indicate a resistive force.
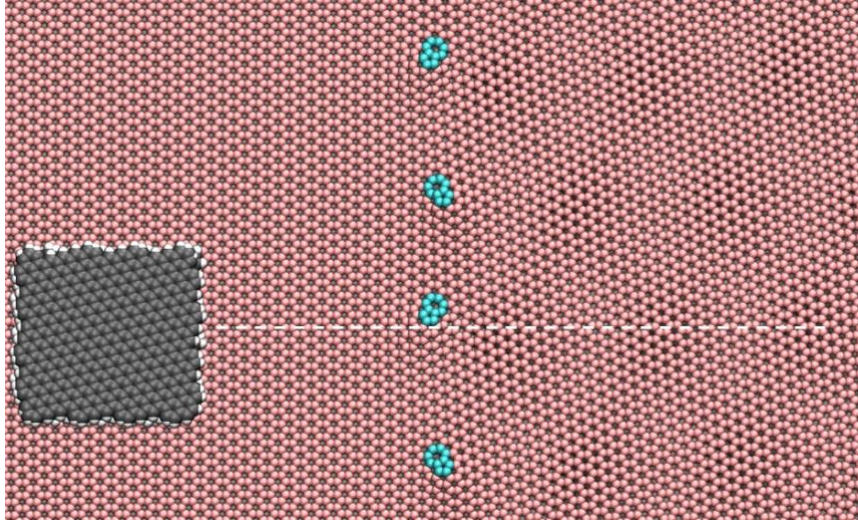

FIG. S15. Illustration showing the orientation of the pentagon-heptagon defects along a $\theta = 4.7°$ GB with respect to the sliding path of the TLG flake. The grey and while spheres represent the carbon and hydrogen atoms of the slider, respectively. The pink and cyan spheres depict the hexagon and dislocation polycrystalline substrate atoms, respectively. The white dashed line depicts the scan line, where the sliding direction is from left to right.

17

12.2. Forward and Backward Sliding over the corrugated $\theta = 13.9°$ GB

The sliding simulation setup for the $\theta = 13.9°$ GB is shown in Fig. S16. For this system, the TLG flake slides simultaneously over two bumps of heights 1.5 Å (bump 1) and 1.4 Å (bump 2). The lateral force traces at different normal loads in the forward sliding direction are shown in the left column of Fig. S17. The corresponding height dynamics of the two bumps is shown in the right column of the figure. Under zero normal load neither of the bumps buckle during the TLG flake crossing of the GB [see panels (a) and (b) of Fig. S17, and SM Movie 5]. A resistive force resulting from the downward bump depression at the simulation time of 0.92-1.12 ns (or sliding distances of 4.6-5.6 nm) followed by enhanced force oscillations and then a negative lateral force due to bump recovery at a simulation time of 1.64-1.8 ns (sliding distances of 8.2-9.0 nm), can be clearly seen. At the normal load of 0.4 GPa [see panels (c) and (d) of Fig. S17, and SM Movie 6], both bumps buckle downward and remain buckled after the TLG flake leaves the GB region. Consequently, the negative lateral force associated with bump unbuckling disappears. The buckling of the bumps leads to the rapid increase of friction observed in the low normal load regime of Fig. 3(c) in the main text. As the normal load is increased to 2.3 GPa, bump 2 unbuckles when the TLG flake leaves the GB region (resulting in the reappearance of a negative lateral force), whereas bump 1 remains buckled [see panels (e) and (f) of Fig. S17, and SM Movie 7]. For normal loads greater than 4.6 GPa, both bumps unbuckle when the TLG flake leaves the GB region [see panels (g) and (h) of Fig. S17, and SM Movie 8].
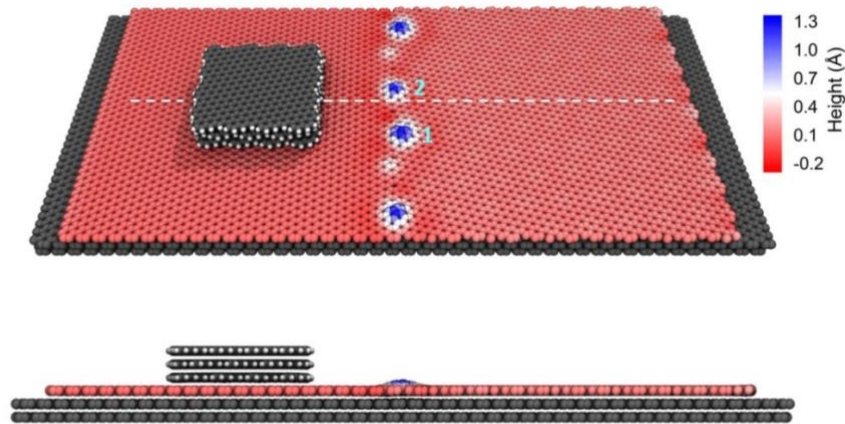

FIG. S16. Sliding simulation setup for the $\theta = 13.9°$ GB. Both perspective (top panel) and front (bottom panel) views are provided. The two bumps in the sliding path, *i.e.* bump 1 and bump 2, are explicitly denoted in the top panel. The grey and white spheres represent carbon and hydrogen atoms, respectively. Coloring of the polycrystalline atoms represents their height with respect to the average height of the two grains (see color scale). The white dashed line depicts the scan line, where the sliding direction is from left to right.

The lateral force traces at different normal loads in the backward sliding direction over the $\theta = 13.9°$ GB are shown in the left column of Fig. S18. A qualitatively similar picture to that found for the forward sliding direction is obtained, where bump 1 and 2 buckle (and remain buckled even after the TLG flake leaves the GB region) at a normal load of 0.4 GPa. Notably, the bumps unbuckle at lower normal loads (1.9 GPa and 2.3 GPa for bump 1 and bump 2, respectively) than those found for the forward sliding. This reflects the asymmetry of the bumps with respect to the GB axis, similar to the case of the $\theta = 4.7°$ GB. See SM Movie 9 for the case of 1.9 GPa normal load.
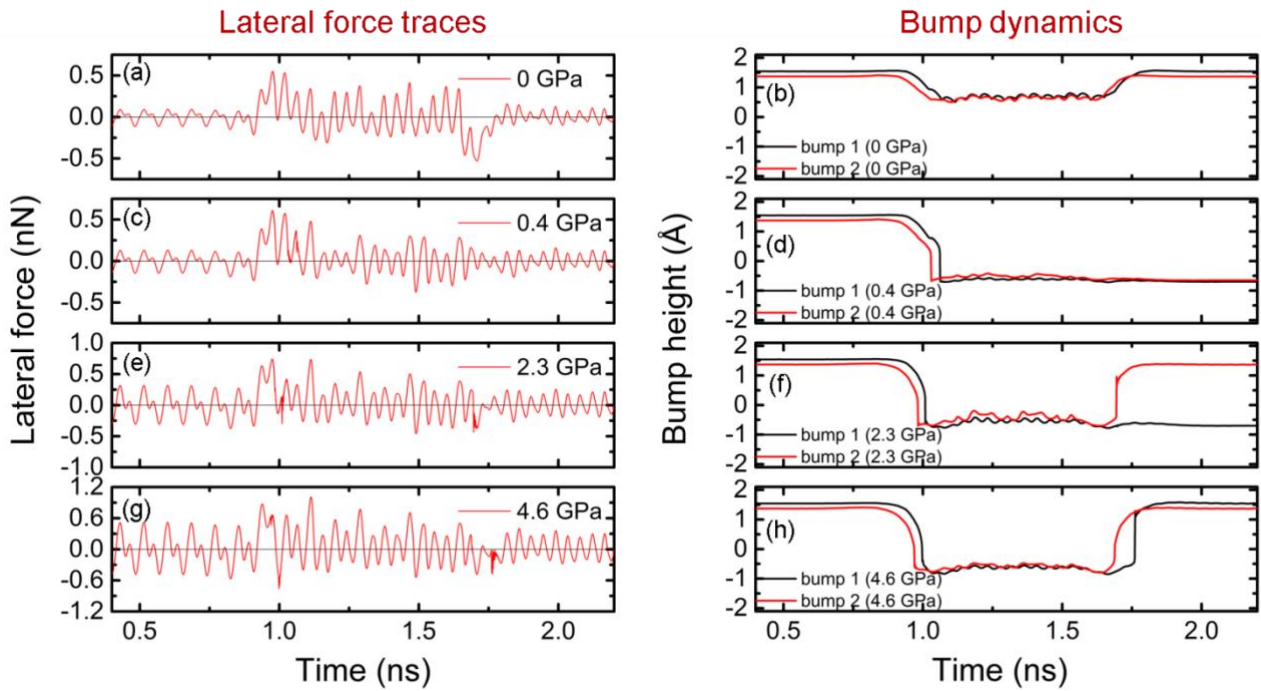

FIG. S17. Lateral force traces and bump dynamics in the forward sliding direction for the $\theta = 13.9°$ GB. Panels (a), (c), (e), and (g) present the lateral force traces as a function of time for normal loads of 0, 0.4, 2.3, and 4.6 GPa, respectively. Panels (b), (d), (f), and (h) show the corresponding bump heights and bump vertical velocities variation profiles. Positive values indicate a resistive force.
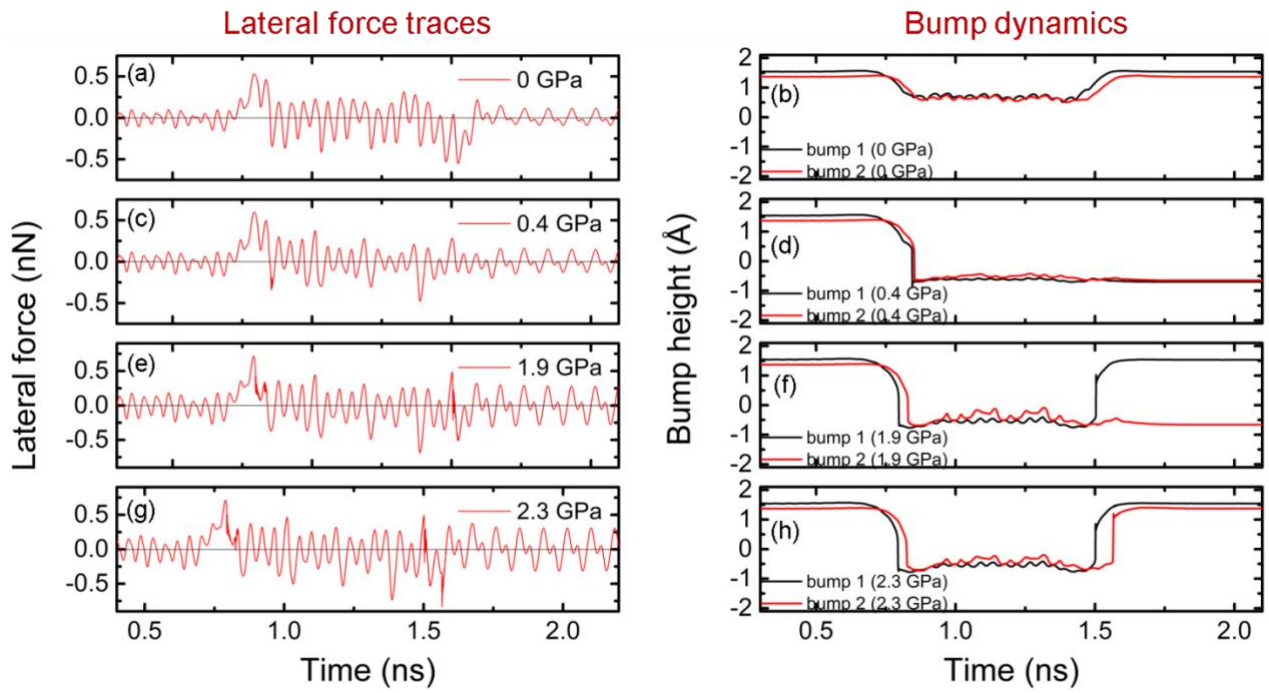
FIG. S18. Lateral force traces and bump dynamics in the backward sliding direction for the $\theta = 13.9°$ GB. Panels (a), (c), (e), and (g) present the lateral force traces as a function of time for normal loads of 0, 0.4, 1.9 and 2.3 GPa, respectively. Panels (b), (d), (f), and (h) show the corresponding bump heights and bump vertical velocities variation profiles. Positive values indicate a resistive force.

12.3. Forward and Backward Sliding for the flat $\theta = 27.8°$ GB

The sliding simulation setup for the $\theta = 27.8°$ flat GB is shown in Fig. S19. The range of the color scale is set to clearly demonstrate the small atomic height difference (~0.07 Å) between the two grains. The simulation protocol is same as that for the $\theta = 4.7°$ and 13.9° GBs. The lateral force traces at different normal loads in the forward (left column) and backward (right column) sliding directions are shown in Fig. S20. In contrast with the corrugated GBs discussed above, the lateral force traces do not exhibit the typical signatures of bump buckling and unbuckling regardless of the applied normal load (see SM Movie 10). The various force trace patterns observed along the sliding path result mainly from the different registry matching between the TLG flake bottom layer and the various polycrystalline regions (Grain 1, Grain 2, and the GB). Notably, the forward and backward force traces are nearly inverted images of each other in this case.
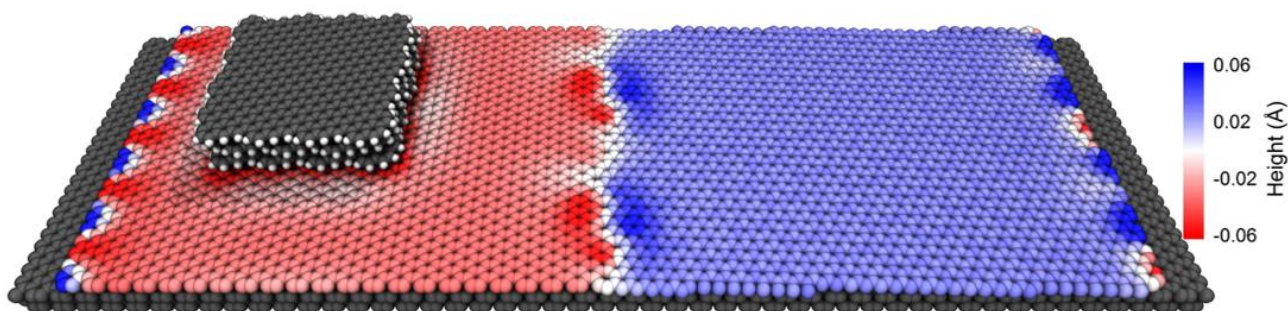

FIG. S19. Sliding simulation setup for the $\theta = 27.8°$ GB. The grey and white spheres represent carbon and hydrogen atoms, respectively. Coloring of the polycrystalline atoms represents the atomic height with respect to the average height of the two grains (see color scale).
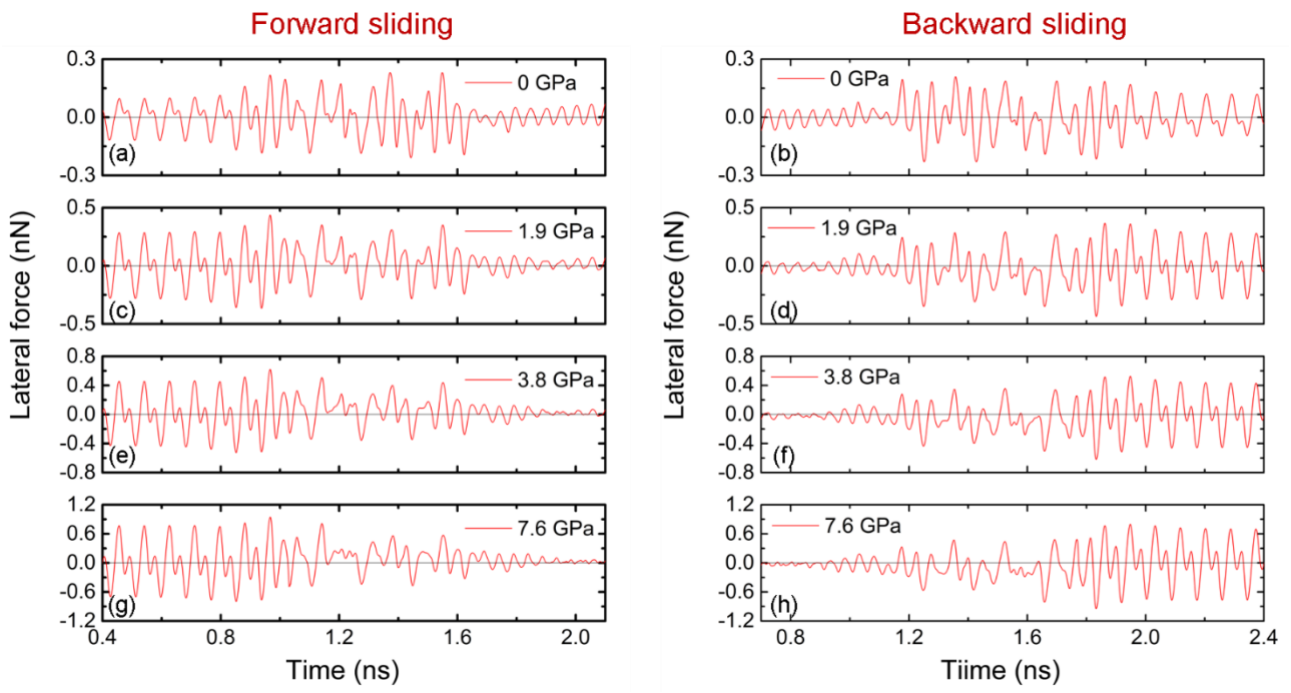
FIG. S20. Lateral force traces along the forward (left panels) and backward (right panels) sliding direction for the $\theta = 27.8°$ GB at normal loads of (a), (b) 0; (c), (d) 1.9; (e), (f) 3.8; and (g), (h) 7.6 GPa.

12.4.   Sliding Simulation for a Pristine Graphene Substrate

The sliding simulation setup for a pristine graphene substrate, shown in Fig. S21(a), is built by replacing the polycrystalline graphene layer with a periodic pristine graphene. The same simulation protocol for sliding on the polycrystalline graphene substrates was used. The sliding simulation for each normal load was conducted for 1 ns. As an example, the lateral force trace for a normal load of 0.8 GPa is shown in Fig. S21(b), showing well defined periodic behavior with the periodicity of the graphene lattice in armchair direction (4.26 Å). The friction force is calculated by averaging the lateral forces at steady-state over six force oscillation periods [e.g. the interval between the dash lines in Fig. S21(b)], neglecting the initial transient dynamics.
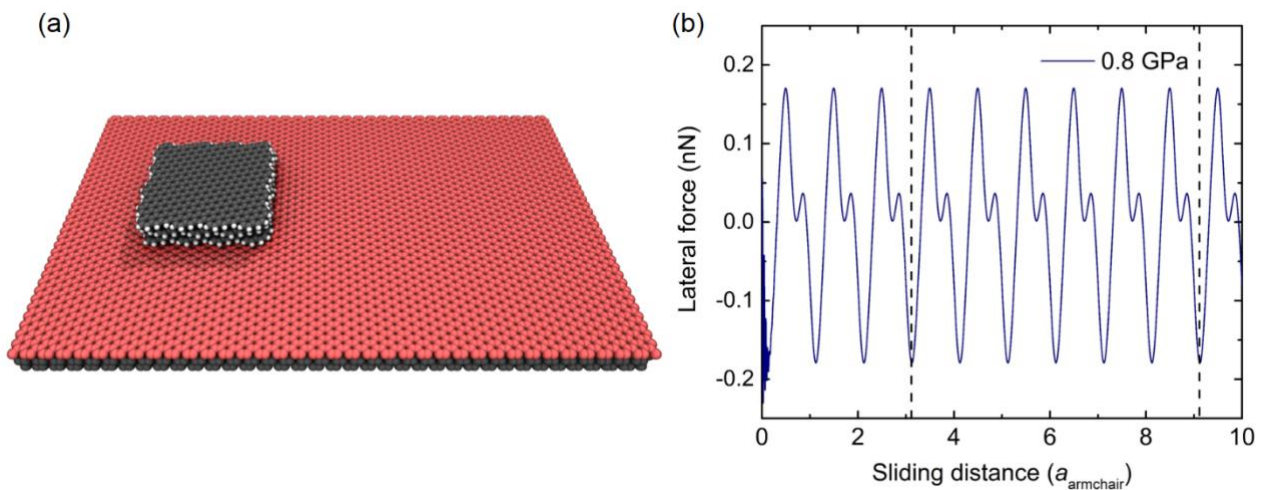

FIG. S21. Simulations of friction over a pristine graphene substrate. (a) Simulation setup. The grey and white spheres represent carbon and hydrogen atoms, respectively. The top substrate layer is colored in red for clarity of the presentation. (b) Lateral force trace at a normal load of 0.8 GPa. The sliding distance is normalized by the periodicity of the graphene lattice in the armchair direction, $a_{armchair} = 4.26$ Å. The dash lines mark the region for lateral force averaging.

23

13. Potential Energy Analysis

13.1. Comparison between Dynamic Simulations and Static Potential Energy Mapping

The static potential energy mapping of the flat GBs was performed by placing TLG flake at different positions along the sliding path and relaxing the system under an external normal load while freezing the lateral motion of the top TLG flake layer. These calculations provide a good representation of the potential energy profile along the sliding path. However, to obtain the fine details of the full energy profile, many calculations are required (see Fig. S22). A more efficient way (in lack of massive parallelization capabilities) to obtain the energy profile is to follow the potential energy component during the dynamical sliding simulation. To verify that both methods indeed provide a similar potential energy profiles and that dynamical effects are negligible in this respect, we compared the energy profiles obtained via static and dynamic calculations at several representative normal loads. An example of one such comparison for a normal load of 3.8 GPa is given in Fig. S22, showing excellent agreement between the static (full black squares) and dynamic (full blue triangles) results. Finally, we present also representative results of quasi-static sliding simulations over Grain 1 and the GB regions (full red circles), where the top layer of the TLG flake is repeatedly shifted followed by structural relaxation of the whole system keeping the lateral position of the top layer fixed. Here, as well, excellent agreement between the quasi-static results and the results of the dynamic simulations is found. Therefore, we conclude that it is safe to employ dynamic simulation results for the potential energy analysis.
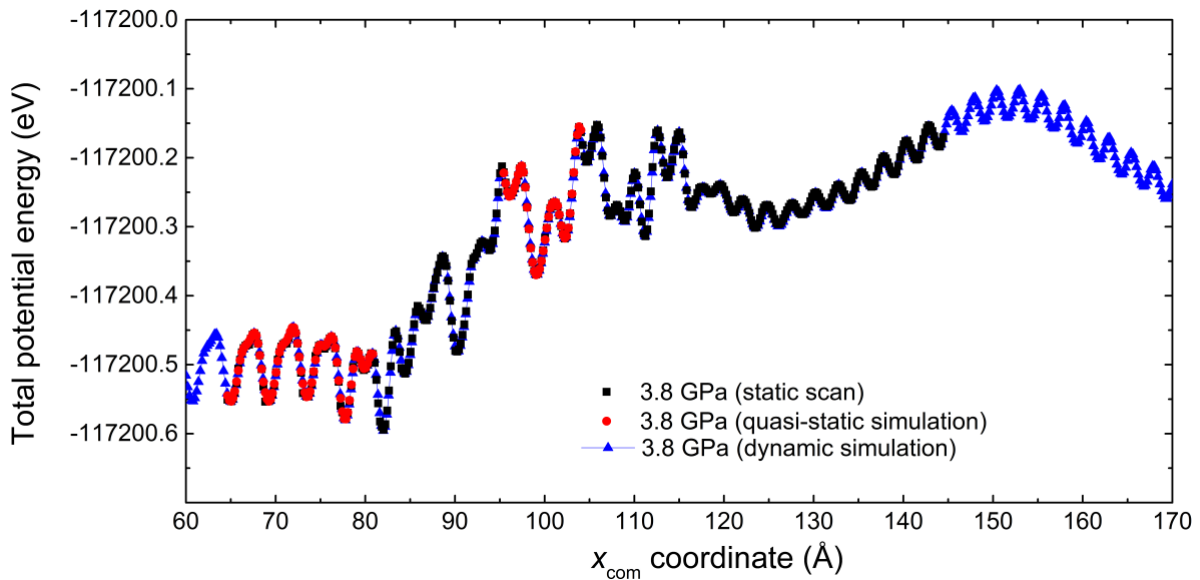

FIG. S22. Comparisons of potential energy profiles obtained by the static scan (full black square), quasi-static calculations (full red circles), and dynamic simulations (full blue triangle), as a function of the center of mass position of the top layer of the flake for the flat $\theta = 27.8°$ GB at a normal load of 3.8 GPa.

13.2. Potential Energy Components for the Flake and the Interface of the $\theta = 27.8°$ GB

The potential energy profiles of the flake and the interaction energy between the flake and the substrate, calculated from dynamic simulations when crossing the GB, are shown in Figs. S23-S24, respectively. The potential profiles of the flake show minor differences between the two grains and are insensitive to the normal load. The interaction energy shows an energy difference of ~0.1 eV between the two grains, which is insensitive to the normal load, as well. Since both contributions do not vary with normal load, our discussion regarding the load dependence friction mechanism in the main text excluded these two terms and focused on the substrate elastic energy contribution.
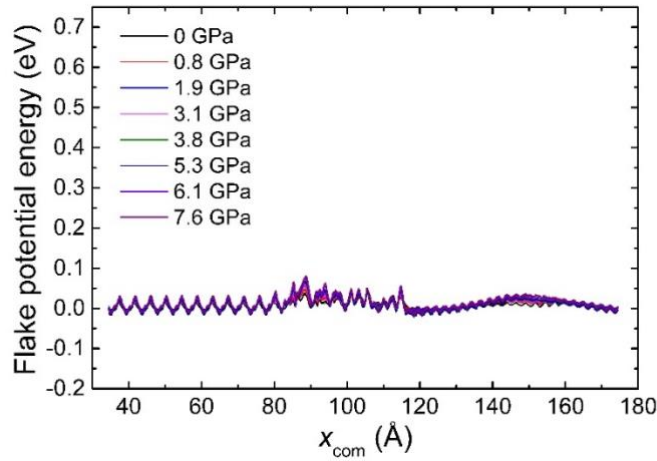

FIG. S23. The potential energy profiles of the flake crossing the $\theta = 27.8°$ GB as a function of the center of mass position of the top layer of the sliding flake at different normal loads. For comparison purposes, the substrate potential energy under each normal load when the flake is positioned deep inside Grain 1 is set to zero.
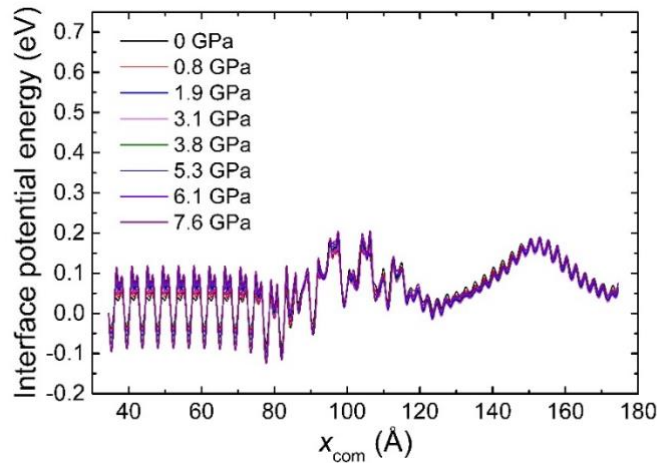

FIG. S24. The interaction energy profiles of the flake-substrate interface for when crossing the $\theta = 27.8°$ GB as a function of the center of mass position of the top layer of the sliding flake at different normal loads. For comparison purposes, the substrate potential energy under each normal load when the flake is positioned deep inside Grain 1 is set to zero.

14. Sensitivity Analysis of the Damping Rate Applied to the Top Layer of the Flake

In the dynamic simulations presented through this study, we applied damping to the vertical motion of the top layer of flake to suppress exaggerated vertical oscillations of the slider while crossing the GB. In experimental scenarios such oscillations are naturally suppressed by energy dissipation to the various components of the measurement setup. To this end, we adopt a damping coefficient of 1.0 ps^{-1}, same as that applied to all degrees of freedom of the middle layers of the substrate and the slider. To verify that this choice of damping coefficient has minor effect on the obtained results we repeated our simulations for the slider crossing the $\theta = 4.7°$ GB under a normal load of 0.8 GPa using a damping rate of 0.1 ps^{-1}. Fig. S25 presents the vertical force acting on the top TLG flake layer clearly showing that the force fluctuations during the bump buckling and unbuckling events indeed decay slower with decreasing damping rate, as expected. Notably, as can be seen in Fig. S26 the lateral force measured during this process is practically insensitive to the choice of vertical motion damping rate within this parameter range, typically used in friction simulations.
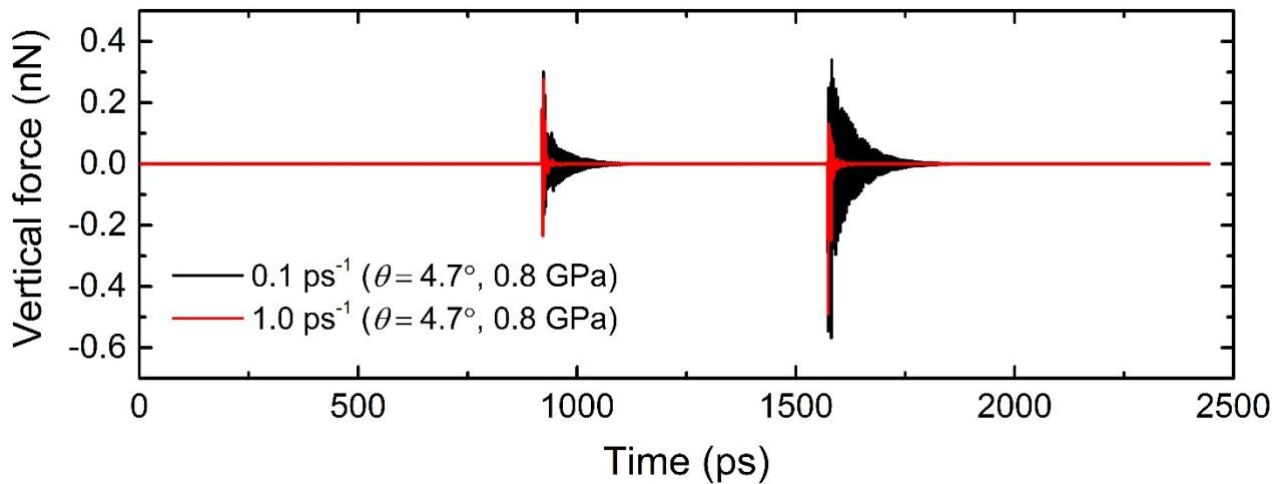

FIG. S25. Vertical force traces acting on the top layer of the TLG flake sliding over the $\theta = 4.7°$ GB under a normal load of 0.8 GPa using two damping coefficients of 0.1 ps^{-1} (black line) and 1.0 ps^{-1} (red line).
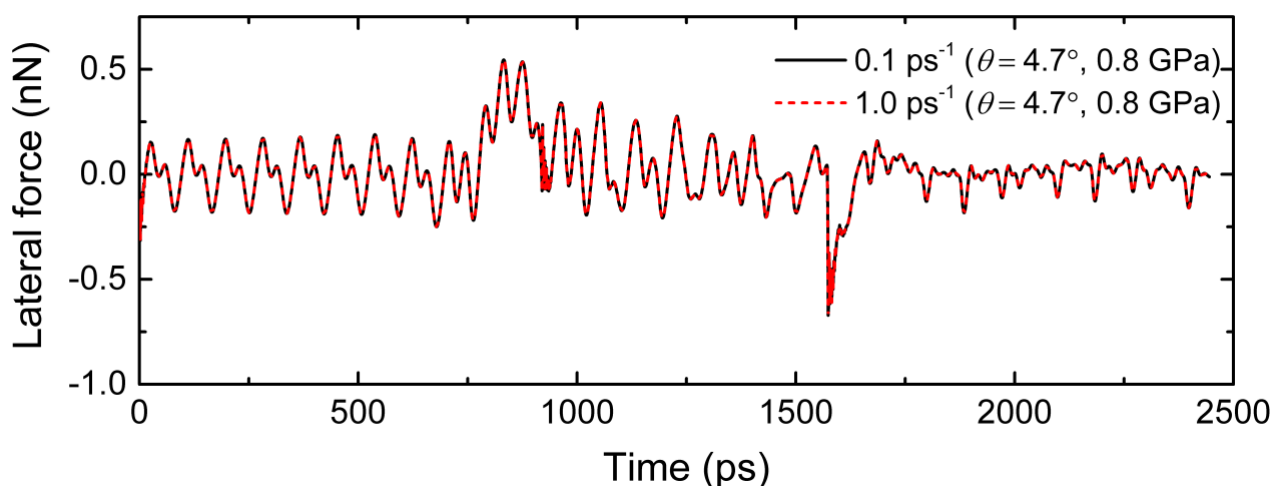
FIG. S26. Lateral force traces acting on a TLG flake crossing the $\theta = 4.7°$ GB system under a normal load of 0.8 GPa using two damping coefficients of 0.1 ps^{-1} (solid black line) and 1.0 ps^{-1} (dashed red line).

References:

1. Yazyev, O. V.; Louie, S. G., Topological defects in graphene: Dislocations and grain boundaries. *Phys. Rev. B* **2010**, 81 (19), 195420.

2. Ophus, C.; Shekhawat, A.; Rasool, H.; Zettl, A., Large-scale experimental and theoretical study of graphene grain boundary structures. *Phys. Rev. B* **2015**, 92 (20), 205402.

3. Kim, K.; Lee, Z.; Regan, W.; Kisielowski, C.; Crommie, M. F.; Zettl, A., Grain Boundary Mapping in Polycrystalline Graphene. *ACS Nano* **2011**, 5 (3), 2142-2146.

4. Ouyang, W.; Mandelli, D.; Urbakh, M.; Hod, O., Nanoserpents: Graphene Nanoribbon Motion on Two-Dimensional Hexagonal Materials. *Nano Lett.* **2018**, 18 (9), 6009-6016.

5. Tison, Y.; Lagoute, J.; Repain, V.; Chacon, C.; Girard, Y.; Joucken, F.; Sporken, R.; Gargiulo, F.; Yazyev, O. V.; Rousset, S., Grain Boundaries in Graphene on SiC(000$\bar{1}$) Substrate. *Nano Lett.* **2014**, 14 (11), 6382-6386.

6. Jónsson, H.; Mills, G.; Jacobsen, K. W., Nudged elastic band method for finding minimum energy paths of transitions. World Scientific: **1998**; pp 385–404.

7. Henkelman, G.; Uberuaga, B. P.; Jónsson, H., A climbing image nudged elastic band method for finding saddle points and minimum energy paths. *J. Chem. Phys.* **2000**, 113 (22), 9901-9904.

8. Henkelman, G.; Jónsson, H., Improved tangent estimate in the nudged elastic band method for finding minimum energy paths and saddle points. *J. Chem. Phys.* **2000**, 113 (22), 9978-9985.

9. Nakano, A., A space–time-ensemble parallel nudged elastic band algorithm for molecular kinetics simulation. *Comput. Phys. Commun.* **2008**, 178 (4), 280-289.

10. Maras, E.; Trushin, O.; Stukowski, A.; Ala-Nissila, T.; Jónsson, H., Global transition path search for dislocation formation in Ge on Si(001). *Comput. Phys. Commun.* **2016**, 205, 13-21.